Article

Correlation between the Covalency and the Thermometric Properties of Yb^{3+}/Er^{3+} Codoped Nanocrystalline Orthophosphates

K. Maciejewska, A. Bednarkiewicz, A. Meijerink, and L. Marciniak*

Read Online

ACCESS | 📊 Metrics & More | 📄 Article Recommendations | 🅢🅘 Supporting Information

ABSTRACT: Lanthanide-doped NaYF$_4$ nanoparticles are most frequently studied host materials for numerous biomedical applications. Although efficient upconversion can be obtained in fluoride nanomaterials and good homogeneity of size and morphology is achieved, they are not very predestined for extensive material optimization toward enhanced features and functions. Here, we study the impact of rare-earth metals RE = Y, Lu, La, and Gd ions within Yb^{3+}/Er^{3+} codoped nanocrystalline REPO$_4$ orthophosphates. The enhanced luminescent thermometry features were found to be in relation to the covalency of RE^{3+}−O$^{2−}$ bonds being modulated by these optically inactive rare-earth ion substitutes. Up to 30% relative sensitivity enhancement was found (from ca. 3.0 to ca. 3.8%/K at −150 °C) by purposefully increasing the covalence of the RE^{3+}−O$^{2−}$ bond. These studies form the basis for intentional optimization thermal couple-based luminescent thermometers such as Yb^{3+}-Er^{3+} upconverting ratiometric thermometer.
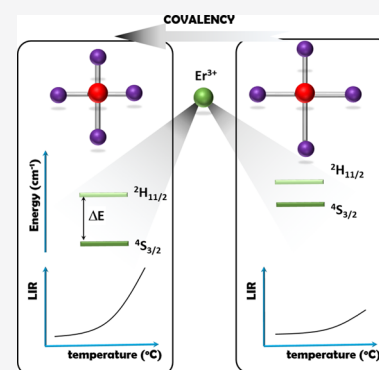
INTRODUCTION

Decreasing the phosphor size to the nanoscale, aiming, for example, to apply it in nano- to biotechnology, often requires studying and understanding of its properties *de novo*, as many new physical processes have been demonstrated to be different in nanoparticles (NPs) as compared to their bulk counterparts.[1] Luminescent NPs exploited for biological applications must meet a number of additional stringent requirements, such as biocompatibility (excluded cytotoxicity), high colloidal stability in water, buffers and other physiological media, and chemical and physical resistance to biofluids,[2] as well as they should exhibit good photoluminescence properties (i.e., lack of photobleaching or photoblinking effects).[3,4] Among many different types of materials used for biorelated applications, the inorganic NPs doped with optically active lanthanide ions seem to satisfy all of the abovementioned requirements. Therefore, they find numerous applications in targeted therapies, for example, in photodynamic therapy, in light-induced photothermal therapy, and in thermal sensing (luminescent thermometry, LT).[5−9] However, biomedical sensing and especially biomedical imaging are hampered by intense autofluorescence and light scattering by tissues or biological media because the spatial resolution or observation depths are compromised. As demonstrated by del Rosal et al.,[10] even when the emission bands of near-infrared (NIR) spectral range, that is, the optical transparency window, are considered, it does not completely eliminate autofluorescence. The solution for this issue, especially usable in the case of in vitro applications, is the upconversion process, in which two or more NIR photons are absorbed and efficiently produce a photon of higher energy. In this approach, autofluorescence-free imaging becomes possible.

The upconversion process is exceptionally sensitive to both the host material composition and the environmental conditions. The former aspect imposes the necessity of the intentional design of the stoichiometry of NPs and considering the phonon energy (which affects the nonradiative depopulation of the excited states), local ion symmetry and the interionic distance (which affect the probability of interionic energy transfer), as well as the type and concentration of dopants (which determine the features such as the spectral range of optical response or brightness).[11,12] Therefore, rare-earth fluorides are most often used for upconversion because of their low phonon energy. However, NPs with fluoride residues may not be neutral in terms of cytotoxicity; therefore, well-developed surface biofunctionalization is crucial when it comes to their in vivo applications in the biological system.[13] Unlike fluoride NPs, phosphate-based NPs, microparticles,[14] glasses, and ceramic materials[15,16] revealed high biocompatibility, and thus, they enable direct surface functionalization without additional surface modification. In addition, orthophosphates are highly resistant to different physical (pressure) and chemical (pH) conditions, so their degradation time in tissues is sufficiently long to increase the probability of their removal

from the organism before lanthanide heavy-metal ions are released from the NPs and accumulated in living cells. Finally, through composition modifications, the crystal field, local symmetry, and the splitting of energy terms in lanthanides can be intentionally modified, aiming at optimizing the spectroscopic properties such as brightness and luminescence lifetimes and their application potential such as the thermometric figures of merits.[17]

Among upconverting optical nanothermometers, the temperature probes based on Yb^{3+}-Er^{3+} ion pairs are the most extensively investigated. The principle behind its thermal responsivity involves the emission intensity ratio of thermally coupled $^2H_{11/2}$ and $^4S_{3/2}$ multiplets of Er^{3+} ions. Although Er^{3+}-based luminescent thermometric properties have already been reported for different host materials,[1,10,18−29] systematic correlation between the structural properties of the host material and the thermometric performance of the luminescent temperature probe have, in general, been rarely studied, aiming at intentionally adjusting the thermographic properties of LT. Especially, the influence of the covalency of the metal-oxygen (M−O, in our case, (RE−O)) bond and the crystal field strength (CFS) on the thermometric properties of lanthanide-based LT have never been reported nor discussed in detail. The understanding of this correlation enables the intentional design of new host materials to enhance the relative sensitivity of luminescent thermometers in the desired temperature range.[30−33]

Therefore, the influence of the host material composition of the rare-earth orthophosphate family of compounds $REPO_4$ (RE: Y, Lu, La, Gd) on the performance of the $REPO_4$:Yb^{3+}, Er^{3+} nanocrystalline luminescent thermometer to noncontact temperature readout has been investigated here. The idea of the approach described in this study is schematically presented in Figure 1. The relative sensitivity of the luminescent thermometer based on the thermally coupled levels depends on the energy separation between them. It is well known that the enhancement of the covalency of the M-O distance affects the energy of the f-state multiplets which, as a consequence, leads to the change in the energy separation $^2H_{11/2}$ and $^4S_{3/2}$ states.[34,35] Hence, the relative sensitivity of the Er^{3+}-based

luminescent thermometer can be altered by the host material composition. The conducted research is focused on the understanding how the local coordination and the interionic distance between the rare-earth cations and the oxygen anions affect the thermal response of particular emission band intensities. The performed studies enable the simple and fast selection of the host material based on its structural parameter like the metal-oxygen distance.

■ MATERIALS AND METHODS

Materials. The Yb^{3+}, Er^{3+}-codoped $REPO_4$ NPs (RE: Y^{3+}, Lu^{3+}, La^{3+}, and Gd^{3+}) were synthesized via the precipitation method. All chemicals: ytterbium(III) oxide, Yb_2O_3 (99.99%, Alfa Aesar), europium(III) oxide, Er_2O_3 (99.9%, Alfa Aesar), yttrium(III) oxide Y_2O_3 (99.99%, Alfa Aesar), lutetium(III) oxide Lu_2O_3 (99.99%, Alfa Aesar), lanthanum(III) oxide La_2O_3 (99.99%, Alfa Aesar), gadolinium(III) oxide Gd_2O_3 (99.99%, Alfa Aesar), ammonium dihydrogen phosphate $(NH_4)H_2PO_4$ (98.0%, Alfa Aesar), and polyethylene glycol (99.5%, Chempur) were used without further purification.

Synthesis. A stoichiometric amount of oxides (Y_2O_3, Lu_2O_3, La_2O_3, Gd_2O_3, Er_2O_3, and Yb_2O_3) was diluted using a Teflon-lined autoclave in ultrapure nitric acid to produce nitrates, followed by the evaporation of the excess solution and drying over P_2O_5 in a vacuum desiccator for 1 day. The procedure of the synthesis of $REPO_4$: Yb^{3+}, Er^{3+} (where RE: Y^{3+}, Lu^{3+}, La^{3+}, and Gd^{3+}) NPs contains two steps. The first step consisted of the precipitation of orthophosphates in polyethylene glycol and water solution using $(NH_4)H_2PO_4$ water solution (0.17 mol/L) at 50 °C. In the second step, the slurry was centrifuged and washed three times in water and ethanol. The obtained orthophosphates were aged at 80 °C for 12 h, and after that, they were annealed at 900 °C for 2 h.

Methods. Powder diffraction studies were carried out using a PANalytical X'Pert Pro diffractometer equipped with an Anton Paar TCU 1000 N temperature control unit using Ni-filtered Cu Ka radiation (V = 40 kV, I = 30 mA). Transmission electron microscopy (TEM) images were obtained using a FEI Tecnai G2 20 X-TWIN microscope equipped with a CCD FEI Eagle 2K camera with a high-angle annular dark field (HAADF) detector and an electron gun with a LaB_6 cathode. The FTIR spectra were measured using a Bruker 66/s FTIR spectrometer. Raman spectra were measured via a confocal microscope from Renishaw equipped with a Si CCD camera for detection and 830 nm excitation line. The spectra were taken in the range of 100−3200 cm^{-1} at room temperature under a 100× objective. The spatial resolution was lower than 1 μm.

The temperature-dependent emission spectra were measured using 977 nm excitation lines using a OPOLLETE 355 LD OPO and NIRQuest-Ocean-Optics spectrometer. The temperature of the sample was changed using a THMS 600 heating stage from Linkam (0.1 °C temperature stability and 0.1 °C set point resolution). The photoluminescence decay times and excitation spectra were obtained using a FLS980 fluorescence spectrometer (Edinburgh Instruments) (1800 lines/mm grating blazed at 500 nm).

Results and Discussion. Rare-earth orthophosphates crystallize in several crystallographic structures such as monoclinic, tetragonal, and hexagonal. The hexagonal polymorphic phase is considered to be not the best candidate host for efficient luminescence, owing to the fact it is usually stabilized by the water molecules[36−38] inside in the crystal
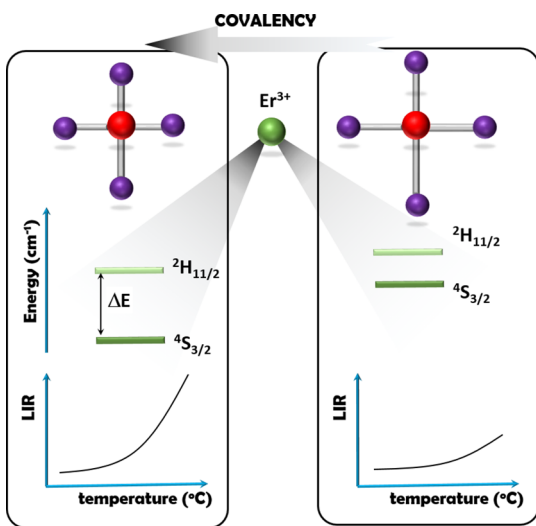
Figure 1. Schematic illustration of the impact of the metal-oxygen bond length on thermal response in luminescent thermometers based on thermally coupled levels .

structure, which are known to quench luminescence. Therefore, the majority of the studies published so far is focused on the tetragonal (high temperature phase) and monoclinic (low temperature phase) orthophosphate polymorphs. For example, YPO_4 and $LuPO_4$ crystalize in the tetragonal xenotime-type structure ($I4_1/amd$) where the rare-earth cations create the REO_8 polyhedrons (Figure 2a). For larger rare-earth ionic
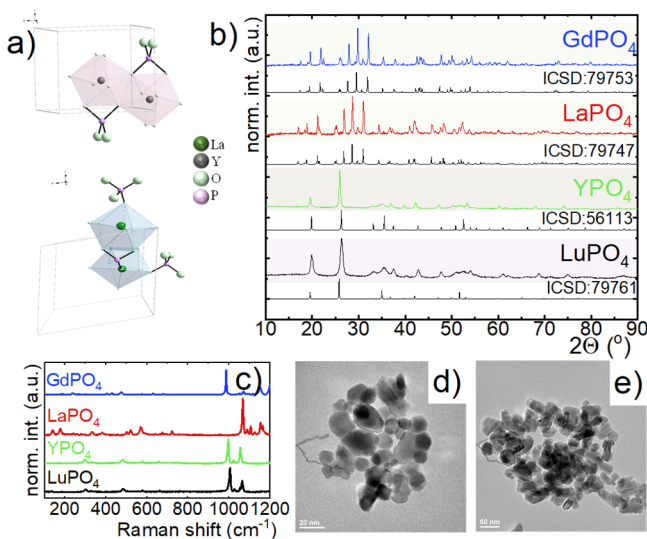
Figure 2. Structure and morphology of $REPO_4$:Yb^{3+}, Er^{3+} (RE; Y, Lu, La, and Gd) materials. The visualization of the unit cells of the YPO_4 and $LaPO_4$ structures (a); XRD patterns of $REPO_4$:Yb^{3+}, Er^{3+} (RE; Y, Lu, La, and Gd) nanocrystals (b); Raman spectra of $REPO_4$:Yb^{3+}, Er^{3+} (RE; Y, Lu, La, and Gd) (c); representative TEM image of the $LuPO_4$ (d) and YPO_4 (e) nanocrystals.

radius, the monazite-type phase is typically obtained. In monazite ($P2_1/n$), the planes are interlinked along the [010] direction which, in consequence, allows the rare-earth atom bind to an additional $O2'$ atom and complete the REO_9 polyhedron (Figure 2b). The observed differences in the coordination and the ionic radii of the rare-earth ions significantly affect the metal-oxygen distance, which is expected to be longer for the monoclinic structure (Table 1). This may strongly modify the optical properties of Ln^{3+}-doped orthophosphates because of the coexistence of two effects: change in the RE−O bond covalency and CFS, whose magnitudes are affected by the $RE^{3+}–O^{2−}$ (RE−O) distance according to the following order: $GdPO_4 > LaPO_4 > LuPO_4 > YPO_4$. The volume of the unit cell decreases analogously. The comparison of the experimental X-ray diffraction (XRD) patterns with the reference patters confirms the phase purity of the obtained nanocrystals (Figure 2b), and the analysis of the TEM images of those nanocrystals reveals that independently of the host material stoichiometry, the spherical nanocrystals of

relatively narrow grain size distribution of the average grain size around 50−60 nm were obtained (Figure 2d,e, Figure S1; the histograms of the particle size distributions are presented in Figure S2). Multiphonon nonradiative transitions are considered as one of the most efficient luminescence quenching processes in Ln^{3+} ions. Therefore, phonon energy of the host matrix should be analyzed in order to understand the luminescent properties of the nanocrystals under investigation. The structural differences of the orthophosphates (e.g., by substituting the cation ions, as proposed here) shall therefore translate to variations in characteristic host material vibrations. Furthermore, high symmetry-selective Raman spectra were measured (Figure 2c), and the maximum phonon energy varied between 1056 and 1155 for YPO_4 and $LaPO_4$, respectively (the maximum phonon energy is listed in Table 1.). The FTIR spectra measured for the $REPO_4$:Yb^{3+},Er^{3+} nanocrystals are presented in Figure S3. The absorption bands with the maxima ~3345 and ~ 1630 cm^{-1} have been observed and assigned to the stretching and bending vibrations for the O−H group. The two bands located at ~624 and ~ 534 cm^{-1} are observed in the ν_4 region of the bending vibrations of the PO_4^{3-} group. The band at ~1041 cm^{-1} can be attributed to the ν_3 anti-symmetric stretching vibration of the PO_4^{3-} group. The peak which occurs at ~530 cm^{-1} corresponds to an internal PO_4 bending mode, while those at lower wavenumbers can be attributed to the lattice vibrations.

The upconversion (UC) process in the Yb^{3+}-Er^{3+} ion pairs is well known and widely described in the literature.[39−42] Therefore, only a brief description of the UC mechanism will be provided here (Figure 3a). Upon the excitation of the sensitizing Yb^{3+} ions by 980 nm radiation, the $^4F_{7/2}$, $^4S_{3/2}$, and $^4F_{9/2}$ states become populated. Their radiative depopulation leads to the occurrence of the two emission bands at 550 nm ($^4S_{3/2} \rightarrow {}^4I_{15/2}$) and 650 nm ($^4F_{9/2} \rightarrow {}^4I_{15/2}$). Because the $^2H_{11/2}$ and $^4S_{3/2}$ states are thermally coupled, at higher temperatures, an additional upconverting emission band appears at 520 nm ($^2S_{3/2} \rightarrow {}^4I_{15/2}$). The $^4I_{11/2}$ state may also be nonradiatively depopulated, which leads to the population of the $^4I_{13/2}$ state. Therefore, an intense emission band at 1550 nm associated with the $^4I_{13/2} \rightarrow {}^4I_{15/2}$ electronic transition is expected in the NIR range of spectra (Figure 3b). The excitation spectra (monitored at λ_{em} = 1550 nm) consist of narrow absorption bands associated with the electronic transition between the energy states of Er^{3+} and the broadband around 950 nm which can be attributed to the $^2F_{7/2} \rightarrow {}^2F_{5/2}$ electronic transition of the Yb^{3+} ions (Figure 3c). The presence of this absorption band in the excitation spectra of the Er^{3+} ions and its high intensity with respect to the Er^{3+} bands confirm efficient $Yb^{3+} \rightarrow Er^{3+}$ energy transfer. It was found that, on average, at room temperature, luminescence decay times measured for λ_{em} = 550 nm ($^4S_{3/2} \rightarrow {}^4I_{15/2}$), λ_{em} = 670 nm ($^4F_{9/2} \rightarrow {}^4I_{15/2}$), and λ_{em} = 1550 nm ($^4I_{13/2} \rightarrow {}^4I_{15/2}$)

Table 1. .Comparison of the Structural Properties of $REPO_4$:Yb^{3+}, Er^{3+} Nanocrystals Based on ICSD 6113 for YPO_4, ICSD 79767 for $LuPO_4$, ICSD 79747 for $LaPO_4$, and ICSD 79753 for $GdPO_4$

matrix	structure type	space group	cell volume (Å)	ionic radius of RE [coordination number] (Å)	RE^a−O^b distance (Å)	max phonon energy (cm^{-1})
YPO_4	tetragonal	$I4_1/amd$	296.01	1.019 [8]	2.24	1056
$LuPO_4$	tetragonal	$I4_1/amd$	278.18	0.977 [8]	2.26	1064
$LaPO_4$	monoclinic	$P2_1/n$	337.20	1.216 [9]	2.36	1155
$GdPO_4$	monoclinic	$P2_1/n$	289.17	1.107 [9]	2.47	1151

^{a}RE: Y, Lu, La, Gd. ^{b}O: the average value of O1 and O2.
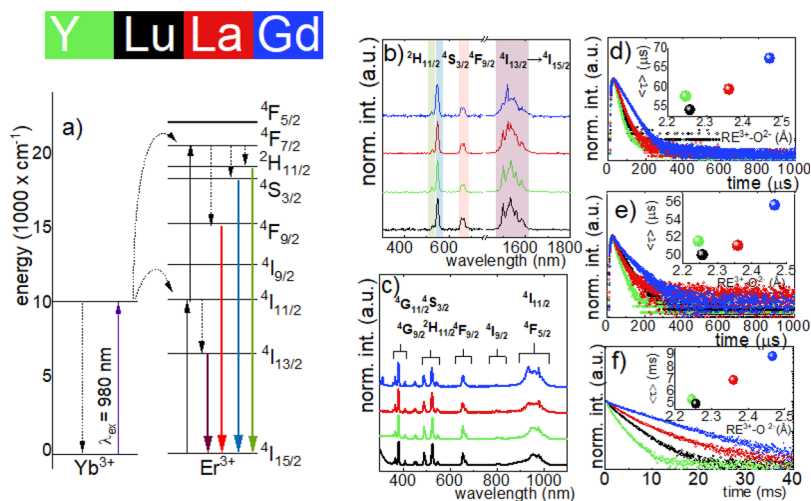
Figure 3. Comparison of the luminescent properties of $REPO_4$:Yb^{3+}, Er^{3+} (RE; Y, Lu, La, and Gd) NPs. Schematic energy level diagram and energy transitions in the Yb^{3+} and Er^{3+} ions (a). Emission (b) and excitation (c) spectra as well as luminescence decay profiles monitored at 550 nm ($^4S_{3/2}$ → $^4I_{15/2}$) (d), 670 nm ($^4F_{9/2}$ → $^4I_{15/2}$) (e), and 1550 nm ($^4I_{13/2}$ → $^4I_{15/2}$) (f). Respective average luminescence decay times are presented in the insets.

increase linearly with the elongation of the RE-O distance (from 54.2 μs, 50 μs, and 5 ms for $LuPO_4$ to 67.5 μs, 56 μs, 8.9 ms for $GdPO_4$ for $^4S_{3/2}$, $^4F_{9/2}$, and $^4I_{13/2}$ states, respectively) (Figure 3d-f). This effect is clearly associated with the probability of multiphonon nonradiative transition and will be discussed in detail later in the manuscript.

In order to fully understand the role of the host material stoichiometry on its thermometric performance, the narrow range (i.e., limited to the $^4I_{15/2}$ → $^2H_{11/2}$ and $^4I_{15/2}$ → $^4S_{3/2}$ electronic transitions of the Er^{3+} ions), low temperature (at 10 K) excitation spectra of the Er^{3+} ions were measured (Figure 4b). As it can be clearly seen, the modification of the host material induces changes in the excitation spectra. First, the splitting between the lowest and the highest Stark components of both multiplets increases sublinearly with the increasing RE^{3+}−O^{2-} distance, and it increases from 228 and 159 cm^{-1} for $LuPO_4$ to 370 and 272 cm^{-1} for $LaPO_4$ for the $^2H_{11/2}$ and
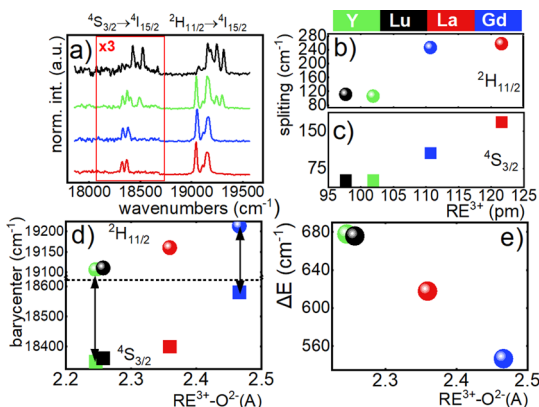
$^4S_{3/2}$ states, respectively (Figure 4b,c). Naturally, the number of Stark components is dependent on the local ion symmetry which changes from dodecahedral for tetragonal host materials (YPO_4, $LuPO_4$) to capped trigonal prismatic for monoclinic ($LaPO_4$ and $GdPO_4$). This is clearly manifested as a higher number of Stark components is observed for the $LaPO_4$:Yb^{3+}, Er^{3+} and $GdPO_4$:Yb^{3+}, Er^{3+} nanocrystals. However, enhanced splitting, in response to the elongation of the RE^{3+}−O^{2-} distance, may be observed even for the host material of the same point symmetry of the RE^{3+} ions. Nevertheless, the magnitude of splitting increases proportionally to the CFS (i.e., proportionally to the ionic radius of substituting ions), independently from the point symmetry of the host material. As the size of all the synthesized NPs is similar, the CFS is responsible for the observed effects.

Additionally, it was found that the mean energies (barycenter) of the $^2H_{11/2}$ and $^4S_{3/2}$ states blue-shift proportionally to the elongation of the RE^{3+}−O^{2-} distance (Figure 4d), which shall be attributed to the reduction of the corresponding covalency of this chemical bond. The magnitude of the shift was higher for $^4S_{3/2}$ (by 120 cm^{-1}) with respect to the $^2H_{11/2}$ one (by 70 cm^{-1}). The difference in the rate of the change of the position of the bands barycenters as a function of the RE^{3+}−O^{2-} distance leads to the lowering of the ΔE energy gap between these two states (Figure 4e). These results clearly indicate that ΔE can be easily and intentionally modulated by the coexisting influence of the covalency of the RE−O bond and the CFS.

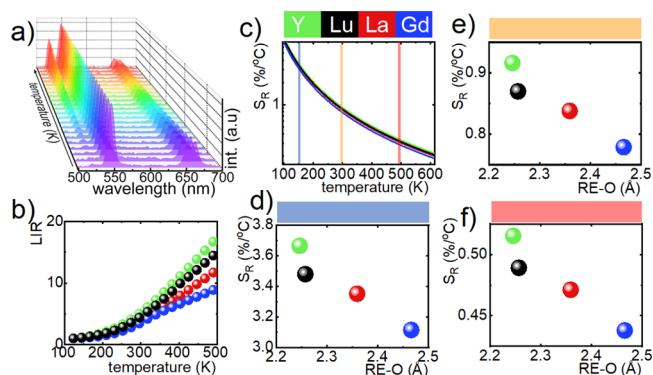Most of the Er^{3+}-based luminescent thermometers take advantage of the luminescence intensity ratio (LIR) of two thermally coupled levels, that is, $^2H_{11/2}$ and $^4S_{3/2}$, which, in the first approximation, can be described by the Boltzmann distribution:

Figure 4. Narrow-range excitation spectra measured at 10 K for $REPO_4$: Yb^{3+},Er^{3+} (λ_{em} = 1550 nm) (a); the influence of the RE^{3+} substitute ion radius on the splitting of the respective $^2H_{11/2}$ (b, circles) and $^4S_{3/2}$ (c, rectangles) multiplets of the Er^{3+} ions; the impact of the RE^{3+}−O^{2-} bond length on the barycenters of $^2H_{11/2}$ (circles) and $^4S_{3/2}$ (rectangles) multiplets (d); and the energy difference between these bands barycenters, ΔE (e) for the $REPO_4$: Yb^{3+},Er^{3+} nanocrystals.

$$LIR_1 = \frac{\int I\left(^4H_{11/2} \rightarrow {}^4I_{15/2}\right)}{\int I\left(^4S_{3/2} \rightarrow {}^4I_{15/2}\right)} = A\frac{g1}{g2}\exp\left(-\frac{\Delta E}{kT}\right) \quad (1)$$

where A, g_i, and k_B describe the pre-exponential parameter, the degeneracy of the given (i-th) energy state, and the Boltzmann constant, respectively. Therefore, as it can be clearly seen in Figure 5a, the increase in temperature induces the enhance-

Figure 5. Representative thermal evolution of the upconverted emission spectra of the YPO_4:Yb^{3+},Er^{3+} nanocrystals at λ_{exc} = 976 nm excitation (a); thermal dependence of LIR (b) and relative sensitivity (c) for different $REPO_4$: Yb^{3+},Er^{3+} nanocrystals; the RE^{3+}–O^{2-} distance (host variable)-dependent S_R at −150 °C (d), 300 °C (e), and 500 °C (f). Color coding of the samples is unified for the (b–f) graphs.

ment of the $^2H_{11/2} \rightarrow {}^4I_{15/2}$ emission intensity with respect to the $^4S_{3/2} \rightarrow {}^4I_{15/2}$ one. Although Yb-Er upconverting thermometers are most frequently studied and most well known, the influence of the covalency of the RE^{3+}–O^{2-} bond and CFS on the thermometric performance of Er^{3+}-based nanothermometers was not studied in detail up to date. As it has already been reported, the relative sensitivity of this type of luminescent thermometers may be affected by the size of the nanocrystals and excitation density.[21,43] Therefore, in order to eliminate these experimental factors and keep the performed analysis reliable, the luminescent properties of NPs of very similar morphologies and sizes were analyzed at low excitation densities (<1.5 W/cm^2). As shown in Figure 5b, the increase in temperature leads to a gradual increase in the $^2H_{11/2} \rightarrow {}^4I_{15/2}$ emission band intensity with respect to the $^4S_{3/2} \rightarrow {}^4I_{15/2}$ one, causing a gradual enhancement of the LIR at elevated temperatures (Figure 5b). However, the rate of thermally enhanced LIR values is strongly dependent on the host material stoichiometry. As was found by many researchers and discussed recently by Suta et al.,[44] the relative emission intensities of the 520 and 550 nm emission bands are governed by the Boltzmann distribution only in a limited temperature range. In order to determine the usable temperature range where the Boltzmann process describe the observed properties well, the ln(LIR) has been plotted against $1/T$ (Figure S3). As expected, above $1/T$ = 0.004 (T = 250 K), there is a significant deviation from the linear trend that suggests that the Boltzmann distribution analysis remains reliable only at temperatures above 250 K. Additionally, based on the Boltzmann fittings, the experimental ΔE was found for all the selected hosts. These values correlated well with the ones obtained from the energy splitting between bands barycenters at low temperatures. The latter is slightly lower than the former because at increased temperatures, higher Stark components of the $^2H_{11/2}$ and $^4S_{3/2}$ multiplets become activated. Nevertheless, the evident decrease of ΔE with the elongation of the RE-O distance can be found in this case. The observed thermally induced changes of LIR are reflected in the relative sensitivity of the luminescent thermometer calculated as follows:

$$S_R = \frac{1}{LIR}\frac{\Delta LIR}{\Delta T} \times 100\%$$

(2)

where ΔLIR corresponds to the change of LIR at ΔT change of temperature. As shown in Figure 5c, S_R has a very similar shape for all the host materials under investigation. It can be clearly seen that independently from the host material stoichiometry, the highest values of S_R are reached at the lowest temperature and gradually decrease at elevated temperatures. It can be also found that RE^{3+}–O^{2-} strongly determines the highest value of S_R, as expected (Figure 5e). Therefore, the highest value of S_R decreases from 3.65%/°C for YPO_4 to 3.1%/°C for $GdPO_4$ nanocrystals at 150 K, while at 300 K, these values decrease from 0.95%/°C for YPO_4 to 0.82%/°C for $GdPO_4$.

The obtained results clearly indicate that the host material composition strongly affects the thermometric performance of the Ln^{3+}-based luminescent thermometers. The coexistence of two effects, namely, the CFS and the covalency of the RE−O bond determines the energy separation and hence the relative sensitivity of the luminescent thermometer based on the emission intensity ratio of two thermally coupled levels. In the considered case, covalence plays the dominant role in modulating energy splitting ΔE as compared to the CFS effect. Therefore, in light of the presented studies, ΔE between two thermally coupled levels and hence the thermometric performance (i.e., sensitivity and brightness) of such a luminescent temperature sensor may be improved by an intentionally increased covalency of the M−O bond.

■ CONCLUSIONS

The upconverting $REPO_4$:Er^{3+}, Yb^{3+} nanocrystals were synthesized using the precipitation method. The systematic investigation of their luminescent properties in a function of temperature indicates the significant role of the host material composition of the thermometric properties of the ratiometric luminescent thermometers based on the intensity ratio of 520 nm ($^2H_{11/2} \rightarrow {}^4I_{15/2}$) to 550 nm ($^4S_{3/2} \rightarrow {}^4I_{15/2}$) emission bands. It was found that the position of the barycenters of these two bands measured at 10 K depends on the RE-O distance. Upon the elongation of this RE-O distance and the resulting decreased covalency, the energy of the $^4S_{3/2}$ multiplet increases faster with respect to $^2H_{11/2}$, and the energy difference ΔE between them decreases linearly. Additionally, the increase in the RE-O distance was found to be an additional factor responsible for the enlargement of the $^2H_{11/2}$ and $^4S_{3/2}$ Stark component splitting. As a consequence, the relative sensitivity of the ratiometric luminescent thermometer based on the emission intensity of the two thermally coupled levels decreases monotonically with the elongation of the RE-O distance. Overall, the obtained results suggest that the low covalency of the RE-O bond and the respective host matrices should be sought, studied, and used to intentionally enhance S_R and to improve the thermometric properties of this type of luminescent thermometers.

■ ASSOCIATED CONTENT

ⓢ Supporting Information

The Supporting Information is available free of charge at https://pubs.acs.org/doi/10.1021/acs.jpcc.0c09532.

> Additional TEM images, NP size distribution histograms, FTIR spectra, and ln(LIR) vs 1/T plots for all the synthesized phosphors (PDF)

◼ AUTHOR INFORMATION

Corresponding Author

    L. Marciniak − *Institute of Low Temperature and Structure Research, Polish Academy of Sciences, 50-422 Wroclaw, Poland;* ⊙ orcid.org/0000-0001-5181-5865; Email: l.marciniak@intibs.pl

Authors

    K. Maciejewska − *Institute of Low Temperature and Structure Research, Polish Academy of Sciences, 50-422 Wroclaw, Poland;* ⊙ orcid.org/0000-0002-8411-3234

    A. Bednarkiewicz − *Institute of Low Temperature and Structure Research, Polish Academy of Sciences, 50-422 Wroclaw, Poland*

    A. Meijerink − *Debye Institute for Nanomaterials Science, Utrecht University Princetonplein 1, Utrecht 3584, The Netherlands;* ⊙ orcid.org/0000-0003-3573-9289

Complete contact information is available at:
https://pubs.acs.org/10.1021/acs.jpcc.0c09532

Notes

The authors declare no competing financial interest.

◼ REFERENCES

(1) Perenboom, J. A. A. J.; Wyder, P.; Festkörperphysik, L.; Meier, F. Electronic Properties of Small Metallic Particles Electronic Properties of Small Metallic Particles. *Phys. Rep.* **1981**, 173−292.

(2) Nune, S. K.; Gunda, P.; Thallapally, P. K.; Lin, Y.; Laird, M.; Berkland, C. J. Nanoparticles for Biomedical Imaging. *Expert Opin. Drug Delivery* **2009**, *6*, 1175−1194.

(3) Hofmann-amtenbrink, M.; Grainger, D. W.; Hofmann, H. Nanoparticles in Medicine : Current Challenges Facing Inorganic Nanoparticle Toxicity Assessments and Standardizations. *Nanomed.: Nanotechnol., Biol. Med.* **2015**, *11*, 1689−1694.

(4) Marciniak, L.; Bednarkiewicz, A.; Kowalska, D.; Strek, W. A New Generation of Highly Sensitive Luminescent Biological Tissues. *J. Mater. Chem. C* **2016**, *4*, 5559−5563.

(5) Okabe, K.; Inada, N.; Gota, C.; Harada, Y.; Funatsu, T.; Uchiyama, S. Fluorescence Lifetime Imaging Microscopy. *Nat. Commun.* **2012**, *3*, 705−709.

(6) Cerõn, E. N.; Ortgies, D. H.; Del Rosal, B.; Ren, F.; Benayas, A.; Vetrone, F.; Ma, D.; Sanz-Rodríguez, F.; Solé, J. G.; Jaque, D.; Rodríguez, E. M. Hybrid Nanostructures for High-Sensitivity Luminescence Nanothermometry in the Second Biological Window. *Adv. Mater.* **2015**, *27*, 4781−4787.

(7) Grzyb, T.; Lis, S. Multifunctional Optical Sensors for Nanomanometry and Nanothermometry: High-Pressure and High-Temperature Upconversion Luminescence of Lanthanide-Doped Phosphates $LaPO_4/YPO_4$:Yb^{3+} − Tm^{3+}. *ACS Appl. Mater. Interfaces* **2018**, *10*, 17269−17279.

(8) Ding, M.; Zhang, M.; Lu, C. $Yb^{3+}/Tm^{3+}/Ho^{3+}$ Tri-Doped YPO_4 Submicroplates: A Promising Optical Thermometer Operating in the First Biological Window. *Mater. Lett.* **2017**, *209*, 52−55.

(9) Wu, Y.; Zhang, Z.; Suo, H.; Zhao, X.; Guo, C. 808 Nm Light Triggered Up-Conversion Optical Nano-Thermometer YPO_4 :$Nd^{3+}/Yb^{3+}/Er^{3+}$ Based on FIR Technology. *J. Lumin.* **2019**, *214*, No. 116578.

(10) Rosal, B.; Villa, I.; Jaque, D.; Sanz-rodríguez, F. In Vivo Autofluorescence in the Biological Windows : The Role of Pigmentation. *J. Biophotonics* **2016**, *9*, 1059−1067.

(11) Monteseguro, V.; Rathaiah, M.; Linganna, K.; Martín, I. R.; Babu, P.; Manjón, F. J.; Jayasankar, C. K.; Venkatramu, V.; Lavín, V. Chemical Pressure Effects on the Spectroscopic Properties of Nd^{3+}-Doped Gallium Nano-Garnets. *Opt. Mater. Express* **2015**, *5*, 7750−7756.

(12) Zhou, Y.; He, X.; Yan, B. Self-Assembled $RE_2(MO_4)_3$:Ln^{3+} (RE= Y, La, Gd, Lu; M = W , Mo ; Ln = Yb/Er, Yb/Tm) Hierarchical Microcrystals : Hydrothermal Synthesis and up-Conversion Luminescence. *Opt. Mater.* **2014**, *36*, 602−607.

(13) Cichos, J.; Kowalczyk, A.; Karbowiak, M. Toxicity Mechanism of Low Doses of Activated Macrophage Cell Lines. *Biomolecules* **2019**, *9*, 20.

(14) Link, D. P.; Van Den Dolder, J.; Van Den Beucken, J. J. J. P.; Cuijpers, V. M.; Wolke, J. G. C.; Mikos, A. G.; Jansen, J. A. Evaluation of the Biocompatibility of Calcium Phosphate Cement / PLGA Microparticle Composites. *J. Biomed. Mater. Res Part A* **2008**, *87A*, 760−769.

(15) Albulescu, R.; Popa, A.; Enciu, A.; Albulescu, L.; Dudau, M.; Popescu, I. D.; Mihai, S.; Codrici, E.; Pop, S.; Lupu, A.; Stan, G. E.; Manda, G.; Tanase, C. Comprehensive In Vitro Testing of Calcium Phosphate-Based Bioceramics with Orthopedic and Dentistry Applications. *Biomaterials* **2019**, *12*, 1−41.

(16) Neel, E. A. A.; Knowles, J. C. *Biocompatibility and Other Properties of Phosphate-Based Glasses for Medical Applications*; Woodhead Publishing Limited, 2009.

(17) Bednarkiewicz, A.; Marciniak, L.; Carlos, L. D.; Jaque, D. Standardizing Luminescence Nanothermometry for Biomedical Applications. *Nanoscale* **2020**, *12*, 14405−14421.

(18) Lojpur, V.; Nikolic, D.; D, M. Luminescence Thermometry below Room Temperature via Up-Conversion Emission of Y_2O_3:Yb^{3+},Er^{3+} Nanophosphors. *J. Appl. Phys.* **2014**, *115*, No. 203106.

(19) Sedlmeier, A.; Achatz, D. E.; Fischer, L. H.; Gorris, H. H.; Wolfbeis, O. S. Nanoscale Photon Upconverting Nanoparticles for Luminescent Sensing of Temperature. *Nanoscale* **2012**, *4*, 7090−7096.

(20) Sanz-rodriguez, F.; Vetrone, F.; Naccache, R.; Zamarro, A.; Juarranz, A.; Fuente, D.; Sanz-rodrí, F.; Maestro, L. M.; Martin, E.; Jaque, D. Temperature Sensing Using Fluorescent Nanothermometers. *ACS Nano* **2010**, *4*, 3254−3258.

(21) Marciniak, L.; Waszniewska, K.; Bednarkiewicz, A.; Hreniak, D.; Strek, W. Sensitivity of a Nanocrystalline Luminescent Thermometer in High and Low Excitation Density Regimes. *J. Phys. Chem. C* **2016**, *120*, 8877−8882.

(22) Savchuk, O. A.; Haro-Gonzalez, P.; Carvajal, J. J.; Jaque, D.; Massons, J.; Aguilo, M.; Diaz, F. Er: Yb : NaY_2F_5O Up-Converting Nanoparticles for Sub-Tissue Fluorescence Lifetime Thermal Sensing. *Nanoscale* **2014**, *6*, 9727−9733.

(23) Wang, K.; Wang, Q.; Yan, T.; Zhao, Q. Thermometers Based on Lanthanide Metal − Organic Framework Materials. *CrystEngComm* **2016**, *18*, 2690−2700.

(24) Kolesnikov, I. E.; Mamonova, D. V.; Kalinichev, A. A.; Kurochkin, M. A.; Medvedev, V. A.; Kolesnikov, E. Y.; Lähderanta, E.; Manshina, A. A. Construction of Efficient Dual Activating Ratiometric YVO_4:Nd^{3+}/Eu^{3+} Nanothermometers Using Co-Doped and Mixed Phosphors. *Nanoscale* **2020**, *12*, 5953−5960.

(25) Wang, L.; Qian, Ã. B.; Chen, H.; Liu, Y.; Liang, A. A Novel Efficient FRET System : $CePO_4$: Tb^{3+} Nanocrystal as Donor and Rhodamine B Dye as Accepter. *Chem. Lett.* **2008**, *37*, 402−403.

(26) Deng, X.; Yu, M.; Zhou, X.; Xia, Z.; Chen, X.; Huang, S. Highly Bright and Sensitive Thermometric $LiYF_4$: Yb, Er Upconversion Nanocrystals Through − Mg^{2+} Tridoping. *J. Mater. Sci.: Mater. Electron.* **2020**, *31*, 3415−3425.

(27) Meijerink, A. $NaYF_4$:Er^{3+},Yb^{3+}/SiO_2 Core/Shell Upconverting Nanocrystals for Luminescence Thermometry up to 900 K. *J. Phys. Chem. C* **2017**, *121*, 3503−3510.

(28) Riwotzki, K.; Meyssamy, H.; Schnablegger, H.; Kornowski, A.; Haase, M. Liquid-Phase Synthesis of Colloids and Redispersible Powders of Strongly Luminescing. *Am. Ethnol.* **2001**, *40*, 573−576.

(29) Meyssamy, H.; Riwotzki, K.; Kornowski, A.; Naused, S.; Haase, M. Wet-Chemical Synthesis of Doped Colloidal Nanomaterials: Particles and Fibers of LaPO$_4$:Eu, LaPO$_4$:Ce, and LaPO$_4$:Ce, Tb. *Adv. Mater.* **1999**, *11*, 840−844.

(30) Hintzmann, W. Absorptionsspektren Des Er^{3+} -Ions in Scandiumvanadat Und Scandiumphosphat Bei Verschiedenen Dotier-ungen. *Z. Physik* **1970**, *224*, 213−224.

(31) Kuse, D. Optische Absorptionsspektren Und Kristallfeldaufspaltungen. *Z. Phys.* **1967**, *58*, 49−58.

(32) Popova, M. N.; Klimin, S. A.; Moiseev, S. A.; Gerasimov, K. I.; Minnegaliev, M. M.; Baibekov, E. I.; Shakurov, G. S.; Bettinelli, M.; Chou, M. C. Crystal Field and Hyperfine Structure of 167 Er^{3+} in YPO$_4$: Er Single Crystals : High-Resolution Optical and EPR Spectroscopy. *Phys. Rev. B* **2019**, *99*, No. 235151.

(33) Rukmini, E.; Devi, A. R.; Jayasankar, C. K. Crystal Free-Ion Energy Level Analysis of Er^{3+} (4f^{11}) in Various Crystal Hosts-Oxygen Coordinated Systems. *Phys. B* **1994**, *193*, 166−176.

(34) Tanner, P. A.; Yeung, Y. Y.; Ning, L. What Factors Affect the ^{5}D$_0$ Energy of Eu^{3+}? An Investigation of Nephelauxetic Effects. *J. Phys. Chem. A* **2013**, *117*, 2771−2781.

(35) Tanner, P. A.; Yeung, Y. Y. Nephelauxetic Effects in the Electronic Spectra of Pr^{3+}. *J. Phys. Chem. A* **2013**, *117*, 10726−10735.

(36) Fang, Y.-P.; Xu, A.-W.; Qin, A.-M.; Yu, R.-J. Selective Synthesis of Hexagonal and Tetragonal Dysprosium Orthophosphate Nanorods by a Hydrothermal Method. *Cryst. Growth Des.* **2005**, *5*, 1221−1225.

(37) Yang, M.; You, H.; Jia, G.; Huang, Y.; Song, Y.; Zheng, Y.; Liu, K.; Zhang, L. Selective Synthesis of Hexagonal and Monoclinic LaPO$_4$:Eu^{3+} Nanorods by a Hydrothermal Method. *J. Crystal Growth* **2009**, *311*, 4753−4758.

(38) Lai, H.; Bao, A.; Yang, Y.; Tao, Y.; Yang, H. Selective Synthesis and Luminescence Property of Monazite- and Hexagonal-Type LaPO$_4$: Eu Nanocrystals. *CrystEngComm* **2009**, *11*, 1109−1113.

(39) Zhu, X.; Feng, W.; Chang, J.; Tan, Y.; Li, J.; Chen, M.; Sun, Y.; Li, F. Temperature-Feedback Upconversion Nanocomposite for Accurate Photothermal Therapy at Facile Temperature. *Nat. Commun.* **2016**, *7*, No. 10437.

(40) Hardman, R. A. Toxicologic Review of Quantum Dots : Toxicity Depends on Physicochemical and Environmental Factors. *Environ. Health Perspect.* **2006**, *114*, 165−172.

(41) Yi, G.; Lu, H.; Zhao, S.; Ge, Y.; Yang, W.; Chen, D.; Guo, L. Synthesis , Characterization , and Biological Application of Size-Controlled Nanocrystalline NaYF$_4$: Yb, Er Phosphors. *Nano Lett.* **2004**, *4*, 2191−2196.

(42) Boyer, J.; Vetrone, F.; Cuccia, L. A.; Capobianco, J. A. Synthesis of Colloidal Upconverting NaYF$_4$ Nanocrystals Doped with Er^{3+} , Yb^{3+} and Tm^{3+} , Yb^{3+} via Thermal Decomposition of Lanthanide Trifluoroacetate Precursors. *J. Am. Chem. Soc.* **2006**, *128*, 7444−7445.

(43) Marciniak, L.; Prorok, K.; Bednarkiewicz, A. Size Dependent Sensitivity of Yb^{3+},Er^{3+} Up-Converting Luminescent Nano-Thermometers. *J. Mater. Chem. C* **2017**, *5*, 7890−7897.

(44) Suta, M.; Antić, Ž.; Dordević, V.; Kuzman, S.; Dramićanin, M. D.; Meijerink, A. Making Nd^{3+} a Sensitive Luminescent Thermometer for Physiological Temperatures — An Account of Pitfalls in Boltzmann Thermometry. *Nanomaterials* **2020**, *10*, 1−20.